Editors' Suggestion

Models of polaron fluctuations in $LuFe_2O_4$

Kristoffer Andreas Holm Støckler,[1,*] Nikolaj Roth,[1] Anders Agentoft Feidenhans'l,[2] Seiya Takahashi,[3] Eiji Nishibori,[3] and Bo Brummerstedt Iversen[1,†]

[1]*Center for Integrated Materials Research, Department of Chemistry and iNANO, Aarhus University, Langelandsgade 140, DK-8000 Aarhus C, Denmark*

[2]*Department of Physics, DTU, Fysikvej 307, DK-2800 Kgs. Lyngby, Denmark*

[3]*Department of Physics, Faculty of Pure and Applied Sciences and TREMS, University of Tsukuba, 1-1-1 Tennodai, Tsukuba, Ibaraki 305-8571, Japan*

(Received 29 November 2023; accepted 28 February 2024; published 29 March 2024)

The structure of $LuFe_2O_4$ below the charge ordering temperature of $T_{CO} = 320$ K has been studied immensely due to the question of whether charge ordering on the mixed valence Fe sublattice leads to a macroscopic electric polarization. In contrast, the local structure associated with polaron fluctuations above T_{CO}, from which the charge ordered structure emerges, is largely unknown. In this work, we characterize this local structure using the x-ray three-dimensional difference pair distribution function (3D-ΔPDF). Atomic correlations extracted directly from the 3D-ΔPDF are used to propose models for the local structure, which are simulated using Monte Carlo methods. It is found that the primary Fourier components of the diffuse scattering can be described by the large, correlated Lu displacements. The local structure of Lu displacements draws conceptual parallels to the classical models of triangular Ising antiferromagnets with the added complexity of interplane interactions. The weaker features of the 3D-ΔPDF are modeled by displacement correlations involving Fe and O, the latter resulting in an increased coordination number of Lu compared with the average structure. Analysis of the Fe-coordination environments in the atomic configurations obtained from Monte Carlo simulations reveals a strong correlation between distortion of the coordination environment and the +II oxidation state of Fe, which suggests a Jahn-Teller polaronic nature of the charge carriers.

DOI: 10.1103/PhysRevMaterials.8.034409

I. INTRODUCTION

$LuFe_2O_4$ has been studied extensively due to the proposed possibility for ferroelectric order arising from charge order on the $Fe^{2+/3+}$ sublattice. Such improper ferroelectricity by charge order could provide strong magnetoelectric coupling due to the direct relation between the charge and spin degrees of freedom, which would be of interest for the application of $LuFe_2O_4$ as a magnetoelectric multiferroic material [1,2]. However, in spite of initial reports of ferroelectric ordering based on pyroelectric current measurements and resonant x-ray scattering [3,4], most of the scientific community studying rare-earth ferrites has reached a consensus, that stoichiometric $LuFe_2O_4$ in fact does not order ferroelectrically [5–8]. The pyroelectric current measurements were instead attributed to extrinsic effects rather than actual ferroelectric ordering [5]. However, $LuFe_2O_4$ is still often cited as a charge order multiferroic material [9] attesting to the many conflicting reports regarding its structure and properties. Such conflicts are not simple to resolve given the complex structural evolution exhibited by $LuFe_2O_4$ with temperature. Above ∼500 K, $LuFe_2O_4$ crystallizes in the $R\bar{3}m$ space group with only the main Bragg reflections being observed in scattering experiments along with a broad diffuse background. In this state, the charges of Fe are considered to be randomly distributed across the Fe sublattice. Between $T_{CO} = 320$ and 500 K, helices of diffuse scattering appear close to the $(\frac{1}{3}, \frac{1}{3}, l)$ lines of reciprocal space while the Bragg scattering indicates the average structure to remain identical to the structure above ∼500 K. For reference, the average structure $R\bar{3}m$ unit cell is shown in Fig. 1(a) along with single crystal x-ray scattering in the (*hhl*) plane at 350 K in Fig. 1(b). Lu is sandwiched between Fe bilayers where each Fe is situated in an approximately trigonal bipyramidal coordination environment, coordinated by O. The emergence of the diffuse scattering has previously been interpreted in terms of the Fe oxidation states forming two-dimensionally ordered layers in the **ab** plane, which stack in a disordered fashion along the **c** direction [3,4,10,11]. Below T_{CO} the helical scattering is observed to condense into satellite reflections with approximate propagation vectors of $(\frac{1}{3}, \frac{1}{3}, \frac{o}{2})$ with o being an odd integer [5]. The appearance of these satellite reflections was interpreted in terms of the onset of three-dimensional charge order of Fe^{2+} and Fe^{3+} [6,10–15]. The location of the satellite reflections in reciprocal space led to the proposition of a commensurately ordered model of Fe oxidation states within each bilayer consisting of two honeycomb ordered layers: one with a surplus of Fe^{2+} and the other with a surplus of Fe^{3+} [10]. This so-called $\sqrt{3} \times \sqrt{3}$ ordering results in the formation of polar Fe bilayers and formed the basis for many of the proposed charge order models in the years to follow [3,4,13]. Based on symmetry analysis, and the observation that the

*kristoffer@chem.au.dk
†bo@chem.au.dk

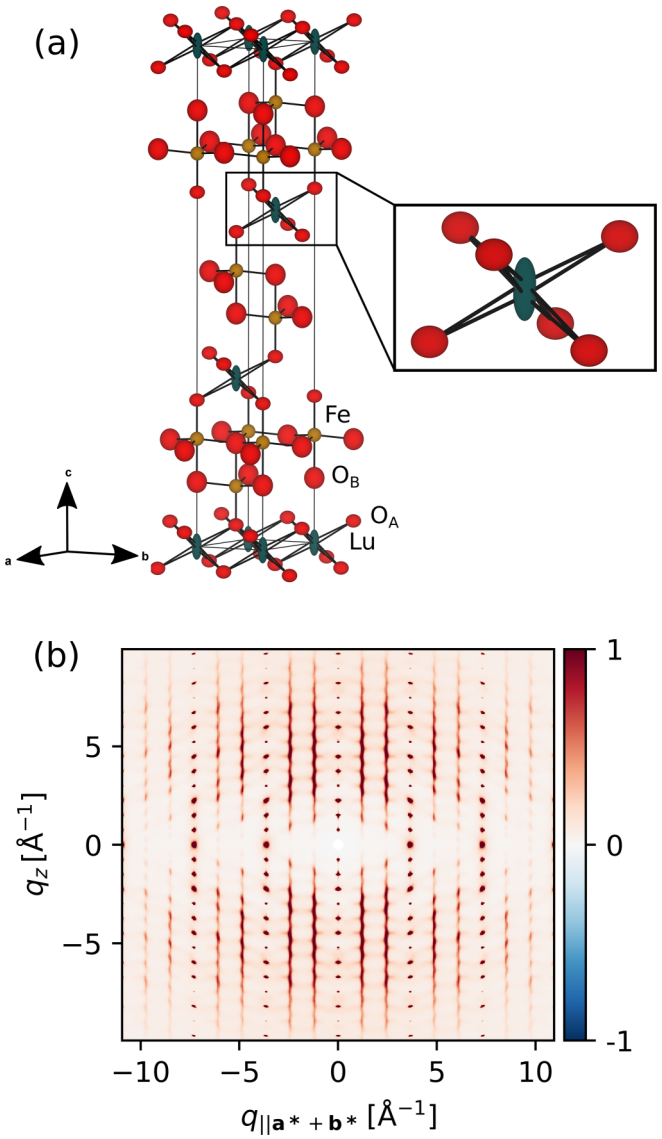

FIG. 1. (a) Average structure of $LuFe_2O_4$ at 350 K as refined against single crystal Bragg diffraction data. The inset shows a close-up of the LuO_6 coordination environment to highlight the split-site Lu position. The figure was drawn using VESTA [20]. (b) Single crystal x-ray scattering in the (*hhl*) plane of reciprocal space. The scattering data is displayed on an arbitrary scale. The negative part of the color bar is included to show that the background subtraction does not result in significant unphysical negative intensities.

intensity variation of the satellite reflections could be explained by the simultaneous presence of three individual monoclinic charge ordered domains, a monoclinic, antiferroelectric structural model for the charge order was proposed [13]. However, this model was later rejected by the same group on the basis of structural refinements against x-ray scattering data from a crystal consisting of almost a single monoclinic domain [6]. The distribution of iron valences in this new structural model was estimated by bond valence sum analysis [16] resulting in a model with charged, apolar bilayers. As such, it was concluded that $LuFe_2O_4$ was not ferroelectric.

While it can be argued that the x-ray, neutron, and electron scattering techniques previously used to characterize $LuFe_2O_4$ are not direct probes of the Fe charge order, these methods are well suited for probing the lattice distortions associated with the charge ordering. These distortions can be considered to arise from the formation of small polarons resulting from the interaction between the charge carriers and the ionic lattice [12]. Estimation of the effective mass of the charge carriers based on spectroscopy is consistent with such a polaron picture with decreased charge hopping below T_{CO} [17,18]. It is notable, that until now the local structure associated with polaron fluctuations above T_{CO} has been largely unknown. Determining this local structure is of interest, since it directly probes the motifs from which the low-temperature charge ordered structure emerges. In the following we use the three-dimensional difference pair distribution function (3D-ΔPDF) to probe this local structure [19]. The 3D-ΔPDF is obtained as the Fourier transform of the isolated diffuse scattering and is equal to the autocorrelation of the difference electron density ($\delta\rho = \rho - \rho_{avg}$, where ρ is the electron density of the crystal and ρ_{avg} is the average periodic electron density). As such, the 3D-ΔPDF will have positive/negative features for interatomic vectors, which separate more/less electron density in the real structure compared to the average structure. Thus, from the 3D-ΔPDF, information on atomic correlations and local structure can be extracted, which is otherwise lost in conventional average structure analysis based on Bragg diffraction data.

From the direct observation of atomic displacement correlations using the 3D-ΔPDF we are able to propose atomistic, structural models for the polaron fluctuations above T_{CO}. Furthermore, by analyzing the proposed models using continuous shape measure (CShM) analysis, we observe distortions of the Fe trigonal bipyramids, which correlate with Fe oxidation states estimated by bond valence sum (BVS) methods. This suggests a Jahn-Teller polaronic nature to the charge carriers.

II. EXPERIMENTAL METHODS

A. Single crystal x-ray diffraction

Single crystal x-ray diffraction was conducted at the BL02B1 beamline at SPring-8 using monochromatic x-ray radiation with a wavelength of 0.24800 Å. Data was collected using a Pilatus 3 X 1 M CdTe detector located 260 mm downstream from the crystal. The data was collected on a $LuFe_2O_4$ single crystal with approximate dimensions of 80 μm at a temperature of 350 K well above the charge ordering temperature. Eight 180° ω scans were performed with $\Delta\omega = 0.2°$ and an exposure time of 0.2 s. Data was collected at detector positions of 0, −10°, −20°, and −30° in 2θ with two χ values of 0 and −45° at each 2θ position. The raw detector frames were converted to Bruker format and integrated using SAINT+ [21]. The data was scaled and corrected for absorption using SADABS [22] and merged using SORTAV [23]. The structure was solved in OLEX2 [24] using SHELXT [25] and refined using SHELXL [26].

B. Single crystal x-ray diffuse scattering

Single crystal x-ray diffuse scattering was collected at the same beamline using the same incident energy and experimen-

tal setup. The detector positions, ω angles, and χ angles were identical to the Bragg diffraction experiment. The exposure time was increased to 0.4 s to ensure good statistics for the weak diffuse scattering signal. The diffuse scattering data was reconstructed in three-dimensional reciprocal space on a $901 \times 901 \times 1001$ voxel grid spanning from -15 to 15 reciprocal lattice units (r.l.u.) in H and K and from -50 to 50 r.l.u. in L (note the $\mathbf{c}^*$ vector is very short due to the long $\mathbf{c}$ axis of the unit cell in direct space) using custom PYTHON scripts. For this process, the orientation matrix was first determined using the Kabsch algorithm [27]. During the reconstruction, averaged air scattering was subtracted from the detector frames and polarization [28] and solid-angle corrections were applied [29]. The reconstructed scattering was symmetrized according to the $\bar{3}m$ point-group symmetry of the Laue class, and Bragg diffraction was punched out and the resulting holes were filled using interpolated values as described by Holm *et al.* [30] inspired by the punch-and-fill method developed by Kobas *et al.* [31]. The diffuse scattering was Fourier transformed in order to obtain the experimental 3D-ΔPDF.

From plots of the diffuse scattering intensity along $(\frac{1}{3}, \frac{1}{3}, l)$ at 300 K shown in Fig. S5 in the Supplemental Material [35], no satellites at $(\frac{1}{3}, \frac{1}{3}, \frac{o}{2})$ positions are observed indicating that charge ordering has not occurred at this temperature. This indicates that our sample is slightly oxygen deficient [5].

III. ANALYZING THE 3D-ΔPDF

Before a detailed analysis of the 3D-ΔPDF is given, it is important to consider what information can be extracted from the average structure refined against the Bragg scattering [Fig. 1(a)]. The Lu site obtains a very large anisotropic displacement parameter indicating disorder. Therefore, inspired by the refinement of the analogous $ErFeMnO_4$ by Nespolo *et al.* [32], the structure was refined with a split-site model for Lu with the occupancy of these two sites refining to 0.510(1), indicating the combined split site to be fully occupied. The two Lu positions are separated by 0.276(1) Å. The splitting of the Lu site indicates a significant disorder component contributing to the Lu position along the **c** axis, which we interpret to be due to the displacement disorder associated with polaron fluctuations. The oxide ions forming part of the LuO_2 layers [labeled O_A in Fig. 1(a)] have unusually large, slightly oblate displacement ellipsoids in the **ab** plane indicating displacement disorder with displacement components predominantly restricted to this plane. On the other hand, the O_B ions, which form part of the Fe_2O_2 bilayer, exhibit displacement ellipsoids that indicate both large in-plane and out-of-plane displacement disorder components. Compared with the O_A ions, the displacement ellipsoids of Fe are more isotropic indicating both in-plane and out-of-plane displacements.

An important point considering the average structure is that the seemingly most disordered sites are the Lu sites. The displacements of Lu along the **c** axis are large enough that the structure is best described by a split-site model. Combined with the fact that the Lu ions have much greater x-ray scattering factors compared with the remaining constituents, it is reasonable to assume that the observed diffuse scattering is mainly due to the Lu disorder. While there is

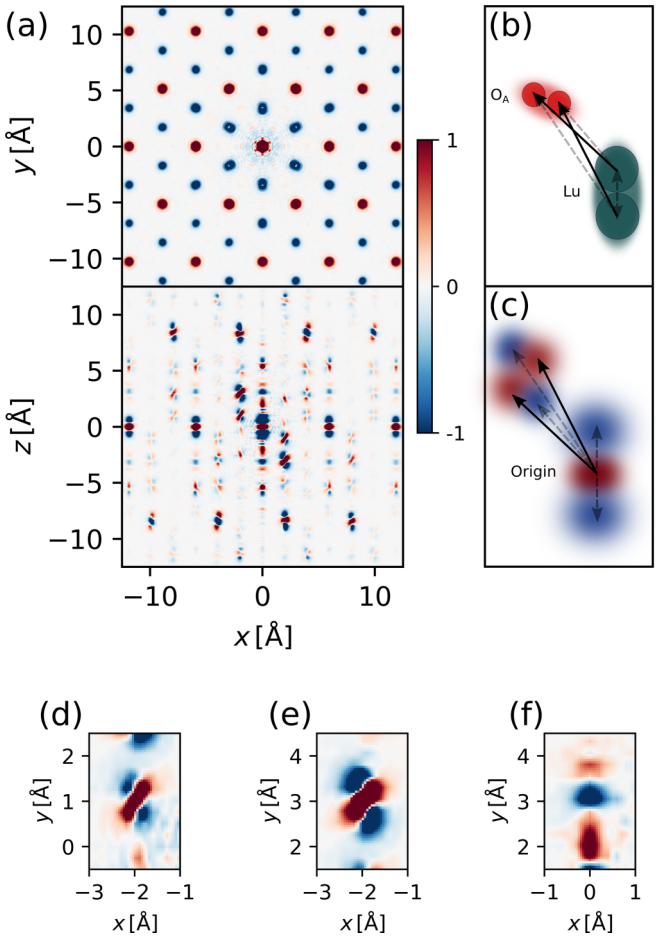

FIG. 2. In (a) the 350 K 3D-ΔPDF in the $xy0$ and $x0z$ planes of Patterson space is shown. Red is positive while blue is negative; the data are shown on an arbitrary scale. The Cartesian x axis is parallel to the $[\bar{2}\ \bar{1}\ 0]$ direction and the z axis is parallel to the $[0\ 0\ 1]$ direction. (b) An illustration of the correlation between the displacements of Lu (green) and O_A (red). The solid-black/dashed-gray vectors are vectors that are more/less frequent in the real structure compared to the average structure. (c) A sketch of the 3D-ΔPDF that would result from the correlated displacements illustrated in panel (b). (d)–(f) show the details of the 3D-ΔPDF features corresponding to (d) the Lu-O_A correlation, (e) the Lu-Fe correlation, and (f) the Lu-O_B correlation discussed in the text.

ample evidence based on resonant x-ray scattering that ordering of Fe oxidation states indirectly contributes to the diffuse scattering [3,4,15], this contribution is weak compared with the contribution of Lu. This point becomes especially clear when considering the 3D-ΔPDF in the $x0z$ plane shown in Fig. 2(a). Here the main characteristics observed are the dumbbell-like features oriented along the **c** direction. The dumbbell features at $z = 0$ in Fig. 2(a) can be attributed to positive displacement correlations with large displacements polarized along the **c** direction of the unit cell. Since Lu is the only ion showing clear signs of such large polarized displacements in the average structure data, the strong features of the 3D-ΔPDF must be largely due to the Lu disorder. Thus, the most significant Fourier components of the diffuse scattering are primarily due to the correlated Lu displacements and not atom pairs involving Fe^{2+}/Fe^{3+}, explaining

why the satellite reflections are dominated by an energy independent contribution when scanning the Fe *K* edge as noted by Mulders *et al.* [15].

From the *xy*0 plane of the 3D-ΔPDF shown in Fig. 2(a) it is observed, that the first nearest neighbor Lu-Lu pair in the **ab** plane exhibits a negative displacement correlation, while the second-nearest neighbor Lu-Lu pair in the **ab** plane exhibits a positive displacement correlation. This trend continues throughout the **ab** plane with negative/positive correlations for odd-/even-order neighbors, respectively. Such a correlation pattern demonstrates a preference for neighboring Lu ions to displace in opposite directions along **c**. This preference is clearly geometrically frustrated on the triangular Lu sublattice. However, the $LuFe_2O_4$ system deviates from the seemingly analogous classical example of the frustrated triangular Ising "antiferromagnet" (TIA), in that positive displacement correlations are also observed between Lu-Lu nearest neighbor pairs along the *z* direction [see Fig. 2(a)]. However, the correlations along *z* die out much quicker than the in-plane correlations, which is consistent with the quasi-one-dimensional nature of the diffuse scattering helices shown in Fig. 1(b). It is noted that for the classical TIA, "antiferromagnet" refers to the effective exchange coupling between neighboring Ising spins while in our case it is rather the effective interaction between the Ising/binary state of either being displaced up or down along the **c** axis.

While the Lu-Lu correlations are responsible for the most intense features of the 3D-ΔPDF observed in Fig. 2(a), many other interesting features can be observed as well. The feature located at (−1.98 Å, 0, 1.03 Å), shown in detail in Fig. 2(d), can be attributed to a positive displacement correlation for the nearest neighbor Lu-O_A pair. This is illustrated in Fig. 2(b). When Lu displaces upwards, the O_A situated above Lu displaces away from Lu to conserve the length of the interatomic vector. Conversely, when Lu displaces downwards, the O_A situated above Lu displaces towards Lu. This results in the two interatomic vectors shown in solid black in Fig. 2(b) being more frequent in the real structure, compared to the average structure resulting in positive features for these vectors in the 3D-ΔPDF as illustrated in Fig. 2(c). On the other hand, the gray, dashed interatomic vectors of Fig. 2(b) will be less frequent in the real structure compared to the average structure giving rise to negative features in the 3D-ΔPDF as illustrated in Fig. 2(c).

As seen from Figs. 2(a) and 2(e) the Lu-Fe nearest neighbor pair shows similar displacement correlations to the Lu-O_A pair; however, the Lu-Fe feature is less canted with respect to the *z* axis compared to the Lu-O_A feature. This is consistent with the observation of the Fe displacement ellipsoid being comparatively more isotropic than the O_A displacement ellipsoid where displacements in the **ab** plane were dominant. The combination of a positive displacement correlation for Lu-Fe nearest neighbor pairs and Lu-Lu nearest neighbor pairs along the *z* direction implies that there should be a positive displacement correlation between the Lu-Fe pair separated by the (0, 0, 5.3 Å) interatomic vector as well. This positive displacement correlation is directly observed in Fig. 2(a) demonstrating the self-consistency of the interpretation of the 3D-ΔPDF. Similarly, a positive feature is observed for the (0, 0, 1.9 Å) interatomic vector that connects nearest neighbor Fe-O_A pairs. This is consistent with a positive displacement correlation implied by their very similar displacement patterns with respect to Lu.

It is interesting to observe that the nearest neighbor Lu-O_B pair exhibits a negative displacement correlation as shown in detail in Fig. 2(f). That is, there is a tendency for the Lu-O_B vector to be either shorter (when Lu displaces towards O_B, O_B tends to displace towards Lu) or longer (when Lu displaces away from O_B, O_B tends to displace away from Lu) than the average structure vector. This shows that locally there is a tendency for Lu to have an effectively higher coordination number of 7 compared to the average structure coordination number of 6.

Having now given a qualitative account of the local structure giving rise to the observed diffuse scattering, we will move on to develop atomistic models, which are consistent with these experimental observations thus probing the structure related to the polarons further.

IV. ATOMISTIC MODELS OF LUTETIUM DISPLACEMENTS

Given that the 3D-ΔPDF method is most sensitive to the Lu displacements, it seems natural to build a model with the Lu disorder as its starting point. In order to construct our atomistic models, we perform Monte Carlo (MC) simulations using the Metropolis algorithm [33] and x-ray scattering is simulated using SCATTY [34]. In the following sections a brief description of the MC simulations is given while a more detailed account is given in the Supplemental Material [35]. It should be noted, that while we choose the Lu disorder as our starting point for modeling the experimental data, the physical origin of the disorder is still considered the polaron fluctuations associated with partial ordering of charges on the Fe sublattice.

From the initial analysis of the 3D-ΔPDF, it is clear that within a single Lu layer, there is a tendency for Lu-Lu nearest neighbors to be displaced in opposite directions. Thus, there should be a term, H_{xy}, taking this into account in the MC Hamiltonian used to simulate the Lu configurations. Furthermore, there should be a term, H_z, which favors like displacement states for nearest neighbor Lu-Lu pairs along the *z* direction, thus increasing the dimensionality of the correlated disorder from two dimensional to three dimensional. The interaction captured in this second term should be weaker, of the order of the MC temperature, to account for the observed shorter correlation length along this dimension.

Furthermore, considering the Lu ordering in the low-temperature structure proposed by de Groot *et al.* [6], one might expect a tendency for the Lu up/down displacements to form honeycomblike ordered layers as found in their structural refinements. An illustration of the low-temperature average structure determined by de Groot *et al.* is given in Supplemental Material Fig. S4 along with an illustration of the honeycomb ordering of displacements [35]. In our simulations, honeycomb ordering could be favored by adding a third term, H_L, to the Hamiltonian. Based on these considerations, a Hamiltonian was set up according to the following

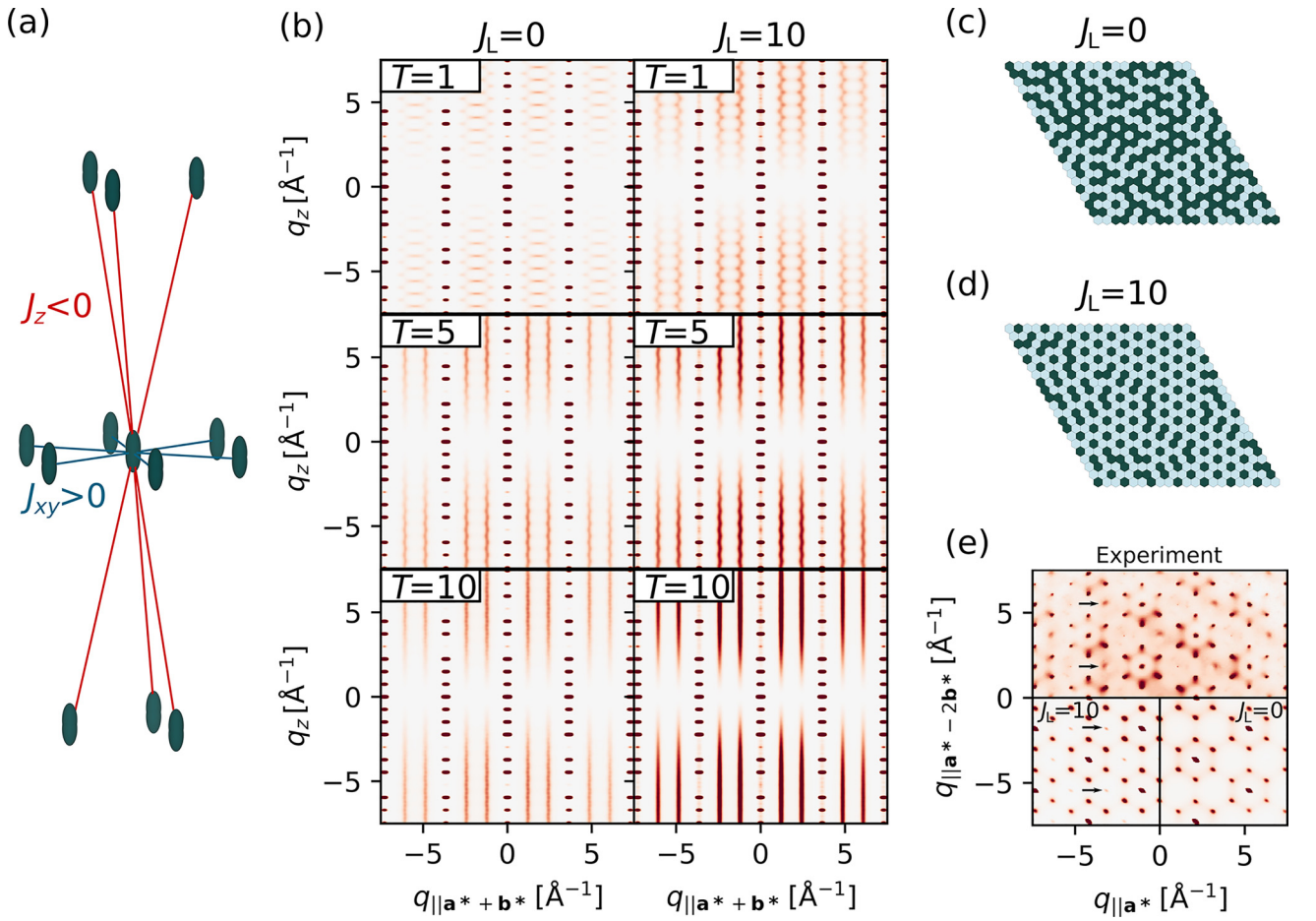

FIG. 3. (a) Illustration of the effective interactions in the model Hamiltonian. J_{xy} is a positive interaction within the individual Lu layers leading to negative correlations for nearest neighbors. J_z is a weak negative interaction between nearest neighbors along the z direction leading to positive correlations between these Lu-Lu pairs. (b) Diffuse scattering resulting from two different values of J_L and three different Monte Carlo temperatures. For all the simulations in this figure $J_z = -1$ and $J_{xy} = 1000$. Scattering simulated with other parameter values is shown in the Supplemental Material [35]. The scattering data is shown on an arbitrary scale. In (c) and (d) two examples cut from representative Lu layers for the simulations with $T = 5$ are shown for $J_L = 0$ and $J_L = 10$, respectively. Dark green and light blue distinguish different Lu-displacement states, either up or down. Regions of partial honeycomb ordering are clearly visible in the $J_L = 10$ layer in (d). In (e) the experimental scattering in the plane spanned by $\mathbf{a}^*$ and $\mathbf{b}^*$ with $l = 17$ is compared to the scattering simulated based on the $J_L = 0$ and $J_L = 10$ models (both with $J_z = -1$, $J_{xy} = 1000$, and $T = 5$). The diffuse maxima observed in the experimental data indicated by arrows are only reproduced by the $J_L = 10$ model.

expression:

$$H = \frac{1}{2}\sum_{i}^{N_{Lu}}\left(J_{xy}\sum_{j\in NN_{xy}}\sigma_i\sigma_j + J_z\sum_{j\in NN_z}\sigma_i\sigma_j\right) + \sum_{i}^{N_L} J_L\left|\left|\sum_{j\in L_i}^{N_{Lu}\in L_i}\sigma_i\right| - \frac{1}{3}N_{Lu}\in L_i\right|.$$

Here σ_i is the displacement state of the ith Lu in the big box, which can assume a value of 1 (displaced in the positive z direction) or -1 (displaced in the negative z direction). The first sum is a sum over all Lu atoms in the big box. Within this sum, a sum is taken over the states of nearest neighbors in the xy plane, which interact with an effective interaction strength of $J_{xy} > 0$ [see Fig. 3(a)]. A summation is also performed over the states of nearest neighbors along the z direction, which interact with an effective interaction strength of $J_z < 0$, which is also illustrated in Fig. 3(a). These sums are the first two terms of the Hamiltonian, H_{xy} and H_z, described above. Finally, the third term is cast in the form of a sum over all N_L Lu layers in the big box and is an energy penalty for layers in which the ratio of Lu atoms displaced up/down to Lu atoms displaced down/up is not 2:1. Within the ith layer, L_i, the absolute value of the sum of all displacement states should equal one-third times the number of Lu ions within L_i, $\frac{1}{3}N_{Lu\in L_i}$, if the states are represented in a 2:1 ratio. The energy penalty is scaled by a parameter $J_L > 0$. It is noted that, while favoring this ratio of states within layers will favor a honeycomblike ordering, one could also have included second-nearest neighbor interactions or other parametrizations to the same effect [36].

X-ray scattering was simulated for various combinations of parameters, including the MC temperature. Scattering for selected parameters of particular interest is shown in Fig. 3(b), and additional examples are included in the Supplemental Material [35]. From Fig. 3(b) it is clear that at low MC temperatures, the weak interlayer coupling along z becomes

increasingly important resulting in a more three-dimensional nature of the diffuse scattering signified by the larger radius of the diffuse scattering helices. On the other hand, the high-temperature region results in the loss of interlayer correlations and therefore a one-dimensional nature of the diffuse scattering. Of particular interest is the intermediate temperature range [$T = 5$ in Fig. 3(b)], where diffuse scattering resembling the experimentally observed helices is produced. It is notable that such diffuse scattering can be found for models with $J_L = 0$ as well as models with $J_L > 0$. In Figs. 3(c) and 3(d) examples of the Lu states in a layer from the $J_L = 0$ and $J_L = 10$ type models with $T = 5$ are shown, respectively. As can be seen from these examples, the local order is very different in these two models while the scattering is qualitatively similar. For the $J_L = 0$ model layers with equal amounts of "up" and "down" states appear to be favored with a local order similar to what would be expected for a conventional TIA ground state. For $J_L = 10$ there is a tendency to have more of one state (up or down) compared to the other, and we observe the formation of clusters of partial honeycomblike order, which is still a ground state for the H_{xy} part of the Hamiltonian. While the scattering shown in Fig. 3(b) shows the qualitative similarity of the $J_L = 0$ and $J_L = 10$ models, the scattering in other planes of reciprocal space distinguish the two models more clearly from one another, which should be expected based on the differences in local order observed from Figs. 3(c) and 3(d). In Fig. 3(e) the experimental scattering is shown in the plane spanned by $\mathbf{a}^*$ and $\mathbf{b}^*$ with $l = 17$. The experimental data exhibits diffuse maxima, indicated by arrows in Fig. 3(e). The $J_L = 0$ model does not reproduce these maxima, whereas they are reproduced by the $J_L = 10$ model. As such, the latter seems to fit better with experiment, which is why one may expect some preference for partial honeycomblike order to be present above T_{CO}.

Furthermore, it is interesting that models with $J_L = 0$ and $J_L > 0$ are able to produce scattering where the diffuse scattering has condensed near the reported $(\frac{1}{3}, \frac{1}{3}, \frac{o}{2})$ satellite positions (see, e.g., the $T = 5$, $J_{xy} = 500$, and $J_L = 100$ model as well as the $T = 10$, $J_{xy} = 100$, and $J_L = 0$ model in Fig. S1 in the Supplemental Material [35]). The models are also able to produce peaks at $(\frac{1}{3}, \frac{1}{3}, l)$ positions (see, e.g., the $T = 10$, $J_{xy} = 1000$, and $J_L = 0$ model in Fig. S1 in the Supplemental Material [35]) where for some samples the diffuse scattering above T_{CO} is observed to exhibit maxima [13]. Our experimental scattering also shows a slight tendency for such peaks at integer l; however, it is not straightforward to conclude which model, $J_L = 0$ or $J_L = 10$, reproduces this most accurately as illustrated by plots of the experimental and simulated intensities along the helices shown in Fig. S5 in the Supplemental Material [35].

It should be noted that the incommensurability of the $(\frac{1}{3}, \frac{1}{3}, \frac{o}{2})$ satellites appears to be best reproduced by the $J_L > 0$ models, which along with the observations made in Fig. 3(e) indicates a structure with an unequal number of up and down states within a single Lu layer to be most likely, consistent with the proposed structural model below T_{CO} [6]. However, it is worth noting that in the structural model reported in [6] the location of the inversion center in between two neighboring Lu layers suggests a negative correlation between the displacements of nearest neighbor Lu-Lu pairs along z while our models assume an interaction, which results in positive correlations for these Lu-Lu pairs consistent with our experimental observations. Considering this inconsistency along with the unresolved disorder indicated by the large atomic displacement ellipsoids still present in the structural refinement by de Groot *et al.*, it appears that the commensurate approximation does not capture the true structure below T_{CO}.

As the diffuse scattering helices above T_{CO} can be reproduced both by the $J_L = 0$ and the $J_L = 10$ models, we shall continue the analysis by using both models as a starting point for developing the atomistic models for the polaron fluctuations.

V. MODELS OF POLARON FLUCTUATIONS

Our atomistic models for the polaron fluctuations use the models of Lu displacements as their starting point. That is, the positions of Fe and O ions are relaxed relative to the displaced Lu ions from the Lu MC simulations. To do this, MC simulations are performed where the effective interactions between relevant ions are mediated by Hooke's law spring potentials [37]. The Fe and O ions are then moved, accepting only moves that lower the energy or result in no change of the energy (corresponding to setting the MC temperature to zero in the Metropolis algorithm). The interactions included in our model are shown in Figs. 4(a) and 4(b). Red lines indicate interactions with simple spring interactions (spring constants $k_{A-B} > 0$) while the blue lines between Lu and O_B indicate interactions where the energy is modified by a size-effect parameter, ϵ, such that energy of a given O_B ion due to the interaction between O_B and the nearest neighbor Lu ion along z is

$$E_{O_B-Lu_{NN_z}} = \frac{k_{O_B-Lu_{NN_z}}}{2}(d_{O_B-Lu_{NN_z}} - (\langle d_{O_B-Lu_{NN_z}}\rangle + \epsilon))^2.$$

Here $k_{O_B-Lu_{NN_z}}$ is the spring constant, $d_{O_B-Lu_{NN_z}}$ the current distance between the ions, and $\langle d_{O_B-Lu_{NN_z}}\rangle$ the distance between the ions in the average structure (the position of Lu in the average structure is assumed to be at the center of mass of the split site). The sign of ϵ depends on the displacement state of the neighboring Lu ion and is chosen such that it ensures a negative displacement correlation as observed in the 3D-ΔPDF. The next-nearest neighbor O_B-Lu interaction was modeled in an analogous way to ensure negative displacement correlations between these pairs as well. The remaining interactions illustrated by the red lines in Figs. 4(a) and 4(b) model positive displacement correlations between ions and thus take the form of classical Hooke's law potentials:

$$E_{A-B} = \frac{k_{A-B}}{2}(d_{A-B} - \langle d_{A-B}\rangle)^2.$$

It should be noted that the effective interactions used for the simulations were selected based on the observed correlations of the 3D-ΔPDF and therefore do not represent actual physical interactions. They are simply a means to generate atomistic configurations consistent with the experimental data. From Figs. 4(a) and 4(b) it is shown that Fe and O_B both have effective interactions with Lu as well as neighboring ions of the same type. These same-type neighbor interactions act as

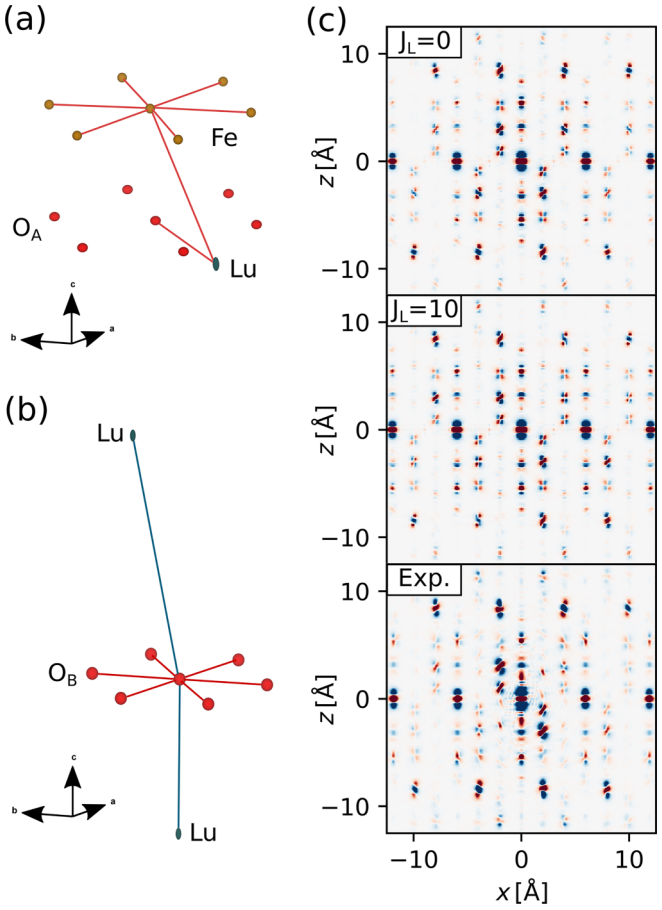

FIG. 4. (a) A sketch of the effective spring interactions between Fe-Lu, Fe-Fe, and O_A-Lu pairs. Red lines indicate classical Hooke's law springs. (b) A sketch of the effective spring interactions between $O_B - Lu_{NN_z}$, $O_B - Lu_{NNN_z}$, and $O_B - O_B$ pairs. The $O_B - Lu_{NN_z}$ and $O_B - Lu_{NNN_z}$ interactions (indicated by blue lines) are modified by an effective size-effect parameter that favors negative displacement correlations for these pairs. (c) $x0z$ planes of the simulated 3D-ΔPDFs based on the $J_L = 0$ and $J_L = 10$ Lu-displacement models and the experimental 3D-ΔPDF.

in-plane stabilizing forces and are imposed to limit in-plane displacements consistent with the displacement ellipsoids observed in the average structure refinements. These stabilizing interactions are omitted for O_A so as not to penalize in-plane displacements consistent with the oblate displacement ellipsoids found for these ions.

In Fig. 4(c) the $x0z$ planes of the simulated 3D-ΔPDFs based on the $J_L = 0$ and $J_L = 10$ ($J_{xy} = 1000$ and $T = 5$) Lu-displacement models are shown along with the experimental 3D-ΔPDF. Both models show very good agreement with the experimental data, which unfortunately does not lend itself well to distinguishing which model ($J_L = 0$ or $J_L = 10$) provides the best atomistic representation of the local structure of the polarons. However, based on the scattering presented in Fig. 3(e), the $J_L = 10$ model seems to reproduce the experimental observations more accurately.

While the two models provided here are clearly different, there are local structural similarities that hint at a peculiar interplay between polarons and orbital degrees of freedom in $LuFe_2O_4$. This will be elaborated in the following section.

VI. ORBITAL ORDER

An interesting aspect of $LuFe_2O_4$ is the approximately trigonal bipyramidal site shared by Fe^{3+} and Fe^{2+}. A perfect trigonal bipyramidal coordination would lead to a splitting of the d-orbital energies as shown in Fig. 5(a). Assuming a high-spin configuration, all orbitals would be singly occupied in the case of Fe^{3+}, while for Fe^{2+} there is an orbital degree of freedom when it comes to selecting into which e'' orbital the additional d-electron goes. Thus, according to the Jahn-Teller theorem, the electron configuration illustrated for Fe^{2+} in Fig. 5(a) would be unstable with respect to a distortion of the coordination environment [38]. As such, one might expect, that the local structure in $LuFe_2O_4$ should reflect this in the disordered state above T_{CO} by favoring distorted coordination environments for Fe^{2+}. Correspondingly, the coordination environment for Fe^{3+} would be expected to be closer to that of a perfect trigonal bipyramid. As demonstrated for the spin-glass material bixbyite, single crystal diffuse scattering allows us to probe this type of local structure [39]. Thus, to investigate this further, the MC simulated atomic configurations used to produce the 3D-ΔPDFs shown in Fig. 5(c) have been analyzed using two different approaches.

In the first approach, the distortion of the Fe trigonal bipyramids was estimated by calculating the CShM for all bipyramids. The CShM provides a number between 0 and 100 that measures the distance between a (centered) polygon and a (centered) reference polygon [40]. Values below 1 are usually interpreted in terms of less significant distortions while higher values indicate important distortions [40]. For our analysis, the reference polygon was chosen to be an FeO_5 trigonal bipyramid from $BaFe_{12}O_{19}$ [41] since this should provide a reasonable estimate for the ideal trigonal bipyramidal coordination environment for Fe^{3+}. The calculation of the CShM was performed using SHAPE v2.1.1 [42]. The resulting values are summarized in the histograms in the leftmost column of Fig. 5(b); the values have been partitioned into two groups based on whether the values are smaller (labeled Fe^{3+}) or larger (labeled Fe^{2+}) than the median value.

The second approach was based on BVS analysis. For each Fe bipyramid the BVS was calculated using the formula [16]

$$V = \sum_i \exp\left(\frac{d_0 - d_i}{0.37\ \text{Å}}\right).$$

Here d_0 is a reference value (here the Fe^{2+} value of 1.734 Å is used since the use of other values did not alter the results significantly) and d_i is the distance between the central ion and the ith ligand. The resulting values are summarized in the histograms in the rightmost column of Fig. 5(b); the values have been partitioned into two groups based on whether the values are smaller or larger than the median value since no obvious way of partitioning the valences could be found by simply inspecting the histograms. The group corresponding to the lowest BVS is assumed to be Fe^{2+} while the group with the highest BVS is assumed to be Fe^{3+}.

Assuming a Jahn-Teller polaronic nature of the mobile charges, one would expect the distribution of dis-

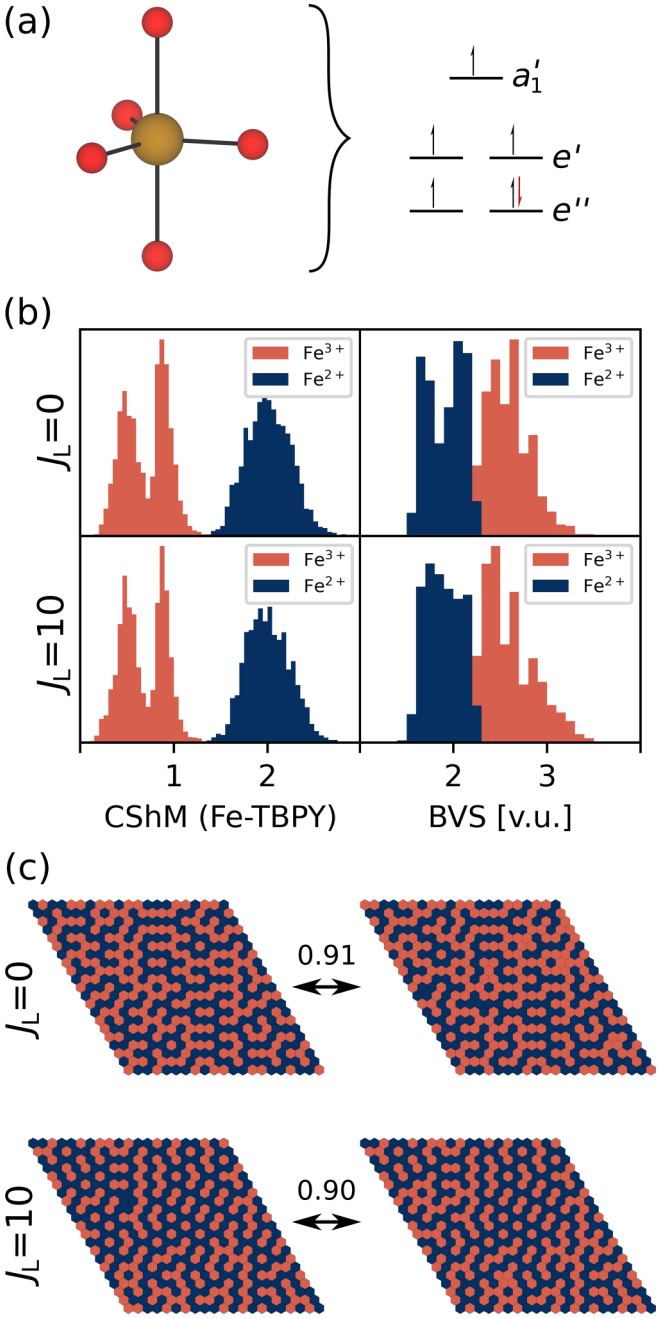

FIG. 5. (a) Illustration of a perfect FeO_5 trigonal bipyramid and an orbital diagram illustrating the splitting of the d-orbital energies in such a crystal field. The black arrows indicate the expected electron configuration for a d^5 ion such as Fe^{3+}. The combination of the red and black arrows shows the expected electron configuration for a d^6 ion such as Fe^{2+}. The figure was drawn using vesta [20]. (b) Histograms of calculated CShM and BVS for the Fe-coordination environments of the big boxes. The partitioning into Fe^{3+} and Fe^{2+} ions is based on the median of the CShM or BVS of all coordination environments. (c) Comparison of representative charge distributions in an Fe layer (orange is Fe^{3+} while blue is Fe^{2+}) estimated based on the CShM (left) and BVS (right) for both the $J_L = 0$ and the $J_L = 10$ models. The number above the arrow is the Pearson correlation calculated for the full big box models.

torted/undistorted sites across the Fe sublattice to exhibit a high correlation with the BVS-estimated Fe^{2+}/Fe^{3+} distribution, and this is in fact also observed. By assigning the distorted and undistorted site values of -1 and $+1$, respectively, and the BVS-estimated Fe^{2+} and Fe^{3+} site values of -1 and $+1$, respectively, we can calculate the Pearson correlation coefficient between the two distributions and find this to be larger than 0.9 for both the $J_L = 0$ and the $J_L = 10$ models [see Fig. 5(c)]. This strong correlation is exemplified in Fig. 5(c) where the assignment of Fe^{2+} and Fe^{3+} (blue and orange) is shown for a representative Fe layer from big boxes of the $J_L = 0$ and $J_L = 10$ models.

While it should be stressed that our models are only in qualitative agreement with the experimental data, these results strongly suggest that the orbital degree of freedom plays a role when it comes to the local structure associated with the polaron fluctuations above T_{CO}. Interestingly, it has previously been found by femtosecond pump-probe spectroscopy that the relaxation rate associated with excitation of polarons and resulting lattice relaxation becomes much slower close to the Néel temperature ($T_N \sim 240$ K) [43]. Such coupling between the polaron dynamics and magnetic order could be expected in the case where orbital degrees of freedom play a role for the polaron dynamics, as our results suggest. However, it should be noted that resonant x-ray scattering and x-ray magnetic circular dichroism experiments do not support long-range orbital order below T_{CO} [15,44].

VII. CONCLUDING REMARKS

The structure and properties of $LuFe_2O_4$ have been studied immensely due to the possibility of improper ferroelectricity arising from charge order on the mixed valence Fe sublattice. Previous studies have mainly focused on the structure below the charge ordering temperature, T_{CO}, where satellite reflections indicate the onset of charge order. In comparison, little effort has been made to understand the local structure associated with the polaron fluctuations above T_{CO} from which the charge ordered structure emerges.

Using the x-ray 3D-ΔPDF method, we directly observe the atomic correlations associated with the polaron fluctuations. The Lu-displacement correlations, which are responsible for the main Fourier components of the diffuse scattering, can be described analogously to a classical triangular Ising antiferromagnet with the addition of short-range interplane correlations. Using Monte Carlo simulations, we reproduce the experimental scattering and 3D-ΔPDF with the weaker features of the 3D-ΔPDF being described by correlations involving Fe and O.

Previously, investigations of the anisotropy of the resonant x-ray scattering signal have been conducted to investigate whether long-range orbital order sets in below T_{CO}. However, the lack of anisotropy to the scattering signal suggested no long-range orbital order to be present. While long-range orbital order appears to be absent in $LuFe_2O_4$ below T_{CO}, our Monte Carlo simulations show a strong correlation between the distortion of the trigonal bipyramidal coordination of Fe and the bond valence sum estimated oxidation states of Fe suggesting a Jahn-Teller polaronic nature of the charge carriers above T_{CO}.

ACKNOWLEDGMENTS

The study was supported by the Villum Foundation (25861). This work was partly financially supported by Japan Society for the Promotion of Science (JSPS) KAKENHI Grants No. JP19KK0132 and No. JP21H05235. The synchrotron experiments were performed at SPring-8 BL02B1 with the approval of the Japan Synchrotron Radiation Research Institute (JASRI) (Proposals No. 2018B0078, No. 2019A0159, and No 2021A1744).

[1] N. A. Spaldin and R. Ramesh, Advances in magnetoelectric multiferroics, Nat. Mater. **18**, 203 (2019).
[2] M. Fiebig, T. Lottermoser, D. Meier, and M. Trassin, The evolution of multiferroics, Nat. Rev. Mater. **1**, 16046 (2016).
[3] N. Ikeda, Ferroelectric properties of triangular charge-frustrated $LuFe_2O_4$, J. Phys.: Condens. Matter **20**, 434218 (2008).
[4] N. Ikeda *et al.*, Ferroelectricity from iron valence ordering in the charge-frustrated system $LuFe_2O_4$, Nature (London) **436**, 1136 (2005).
[5] M. Angst, Ferroelectricity from iron valence ordering in rare earth ferrites? Phys. Status Solidi RRL **7**, 383 (2013).
[6] J. de Groot, T. Mueller, R. A. Rosenberg, D. J. Keavney, Z. Islam, J.-W. Kim, and M. Angst, Charge order in $LuFe_2O_4$: An unlikely route to ferroelectricity, Phys. Rev. Lett. **108**, 187601 (2012).
[7] A. Ruff, S. Krohns, F. Schrettle, V. Tsurkan, P. Lunkenheimer, and A. Loidl, Absence of polar order in $LuFe_2O_4$, Eur. Phys. J. B **85**, 290 (2012).
[8] S. Lafuerza, G. Subias, J. Blasco, J. Garcia, G. Nisbet, K. Conder, and E. Pomjakushina, Determination of the charge-ordered phases in $LuFe_2O_4$, Europhys. Lett. **107**, 47002 (2014).
[9] M. Kumar, S. Shankar, A. Kumar, A. Anshul, M. Jayasimhadri, and O. P. Thakur, Progress in multiferroic and magnetoelectric materials: Applications, opportunities and challenges, J. Mater. Sci.: Mater. Electron. **31**, 19487 (2020).
[10] Y. Yamada, S. Nohdo, and N. Ikeda, Incommensurate charge ordering in charge-frustrated $LuFe_2O_4$ system, J. Phys. Soc. Jpn. **66**, 3733 (1997).
[11] N. Ikeda, Y. Yamada, S. Nohdo, T. Inami, and S. Katano, Incommensurate charge ordering in mixed valence system $LuFe_2O_4$, Phys. B (Amsterdam, Neth.) **241**, 820 (1997).
[12] Y. Yamada, K. Kitsuda, S. Nohdo, and N. Ikeda, Charge and spin ordering process in the mixed-valence system $LuFe_2O_4$: Charge ordering, Phys. Rev. B **62**, 12167 (2000).
[13] M. Angst *et al.*, Charge order in $LuFe_2O_4$: Antiferroelectric ground state and coupling to magnetism, Phys. Rev. Lett. **101**, 227601 (2008).
[14] Y. Horibe, S. Mori, N. Ikeda, K. Yoshii, H. Maeno, and Y. Murakami, Crystallographical and morphological changes in charge-ordering transition of RFe_2O_4(R: Y, Lu) investigated by transmission electron microscopy, Ferroelectrics **584**, 20 (2021).
[15] A. M. Mulders, S. M. Lawrence, U. Staub, M. Garcia-Fernandez, V. Scagnoli, C. Mazzoli, E. Pomjakushina, K. Conder, and Y. Wang, Direct observation of charge order and an orbital glass state in multiferroic $LuFe_2O_4$, Phys. Rev. Lett. **103**, 077602 (2009).
[16] N. E. Brese and M. Okeeffe, Bond-valence parameters for solids, Acta Crystallogr., Sect. B: Struct. Sci., Cryst. Eng. Mater. **47**, 192 (1991).
[17] X. S. Xu *et al.*, Charge order, dynamics, and magnetostructural transition in multiferroic $LuFe_2O_4$, Phys. Rev. Lett. **101**, 227602 (2008).
[18] X. S. Xu, J. de Groot, Q. C. Sun, B. C. Sales, D. Mandrus, M. Angst, A. P. Litvinchuk, and J. L. Musfeldt, Lattice dynamical probe of charge order and antipolar bilayer stacking in $LuFe_2O_4$, Phys. Rev. B **82**, 014304 (2010).
[19] T. Weber and A. Simonov, The three-dimensional pair distribution function analysis of disordered single crystals: Basic concepts, Z. Kristallogr. - Cryst. Mater. **227**, 238 (2012).
[20] K. Momma and F. Izumi, VESTA 3 for three-dimensional visualization of crystal, volumetric and morphology data, J. Appl. Crystallogr. **44**, 1272 (2011).
[21] Bruker, SAINT+ integration engine reference, version 8.38A Q6, Bruker AXS Inc., 2013.
[22] L. Krause, R. Herbst-Irmer, G. M. Sheldrick, and D. Stalke, Comparison of silver and molybdenum microfocus X-ray sources for single-crystal structure determination, J. Appl. Crystallogr. **48**, 3 (2015).
[23] R. H. Blessing, Outlier treatment in data merging, J. Appl. Crystallogr. **30**, 421 (1997).
[24] O. V. Dolomanov, L. J. Bourhis, R. J. Gildea, J. A. K. Howard, and H. Puschmann, OLEX2: A complete structure solution, refinement and analysis program, J. Appl. Crystallogr. **42**, 339 (2009).
[25] G. M. Sheldrick, SHELXT - Integrated space-group and crystal-structure determination, Acta Crystallogr., Sect. A: Found. Adv. **71**, 3 (2015).
[26] G. M. Sheldrick, Crystal structure refinement with SHELXL, Acta Crystallogr., Sect. C: Struct. Chem. **71**, 3 (2015).
[27] W. Kabsch, Solution for best rotation to relate 2 sets of vectors, Acta Crystallogr., Sect. A: Found. Adv. **32**, 922 (1976).
[28] W. Kabsch, Evaluation of single-crystal x-ray-diffraction data from a position-sensitive detector, J. Appl. Crystallogr. **21**, 916 (1988).
[29] M. E. Wall, in *Micro and Nano Technologies in Bioanalysis: Methods and Protocols*, edited by R. S. Foote and J. W. Lee (Humana Press, Totowa, NJ, 2009), p. 269.
[30] K. A. U. Holm, N. Roth, C. M. Zeuthen, K. Tolborg, A. A. Feidenhans'l, and B. B. Iversen, Temperature dependence of dynamic dipole formation in PbTe, Phys. Rev. B **102**, 024112 (2020).
[31] M. Kobas, T. Weber, and W. Steurer, Structural disorder in the decagonal Al-Co-Ni. I. Patterson analysis of diffuse x-ray scattering data, Phys. Rev. B **71**, 224205 (2005).
[32] M. Nespolo, M. Isobe, J. Iida, and N. Kimizuka, Crystal structure and charge distribution of $ErFeMnO_4$, J. Alloys Compd. **313**, 59 (2000).
[33] N. Metropolis, A. W. Rosenbluth, M. N. Rosenbluth, A. H. Teller, and E. Teller, Equation of state calculations by fast computing machines, J. Chem. Phys. **21**, 1087 (1953).

[34] J. A. M. Paddison, Ultrafast calculation of diffuse scattering from atomistic models, Acta Crystallogr., Sect. A: Found. Adv. **75**, 14 (2019).

[35] See Supplemental Material at http://link.aps.org/supplemental/10.1103/PhysRevMaterials.8.034409 for examples of simulated diffuse scattering for other Monte Carlo simulation parameters, a detailed account of the simulations, and illustrations of the low-temperature structure suggested by de Groot *et al*. [6].

[36] H. Ishizuka and Y. Motome, Thermally induced phases in an Ising Kondo lattice model on a triangular lattice: Partial disorder and Kosterlitz-Thouless state, Phys. Rev. B **87**, 155156 (2013).

[37] T. R. Welberry, *Diffuse X-ray Scattering and Models of Disorder* (Oxford University Press, New York, 2022).

[38] H. A. Jahn and E. Teller, Stability of polyatomic molecules in degenerate electronic states. I. Orbital degeneracy, Proc. R. Soc. London **161**, 220 (1937).

[39] K. A. H. Støckler, N. Roth, T. B. E. Grønbech, and B. B. Iversen, Epitaxial intergrowths and local oxide relaxations in natural bixbyite $Fe_{2-x}Mn_xO_3$, IUCrJ **9**, 523 (2022).

[40] J. Cirera, E. Ruiz, and S. Alvarez, Continuous shape measures as a stereochemical tool in organometallic chemistry, Organometallics **24**, 1556 (2005).

[41] A. Krzatala, T. L. Panikorovskii, I. O. Galuskina, and E. V. Galuskin, Dynamic disorder of Fe^{3+} Ions in the crystal structure of natural barioferrite, Minerals **8**, 340 (2018).

[42] M. Llunell, D. Casanova, J. Cirera, J. Bofill, P. Alemany, S. Alvarez, M. Pinsky, and D. Avnir, *SHAPE v2.1.1, Program for the Calculation of Continuous Shape Measures of Polygonal and Polyhedral Molecular Fragments* (University of Barcelona, Barcelona, 2013).

[43] J. Lee, S. A. Trugman, C. L. Zhang, D. Talbayev, X. S. Xu, S. W. Cheong, D. A. Yarotski, A. J. Taylor, and R. P. Prasankumar, The influence of charge and magnetic order on polaron and acoustic phonon dynamics in $LuFe_2O_4$, Appl. Phys. Lett. **107**, 042906 (2015).

[44] K. T. Ko, H. J. Noh, J. Y. Kim, B. G. Park, J. H. Park, A. Tanaka, S. B. Kim, C. L. Zhang, and S. W. Cheong, Electronic origin of giant magnetic anisotropy in multiferroic $LuFe_2O_4$, Phys. Rev. Lett. **103**, 207202 (2009).